Engineering Analysis with Boundary Elements 83 (2017) 229–241

Contents lists available at ScienceDirect

Engineering Analysis with Boundary Elements

journal homepage: www.elsevier.com/locate/enganabound

A high-order three-dimensional numerical manifold method enriched with derivative degrees of freedom

Huo Fan[a,*], Jidong Zhao[a], Hong Zheng[b]

[a] Department of Civil and Environmental Engineering, The Hong Kong University of Science and Technology, Clear Water Bay, Kowloon, Hong Kong
[b] Key Laboratory of Urban Security and Disaster Engineering, Ministry of Education, Beijing University of Technology, Beijing 100124, China

ARTICLE INFO

Keywords:
Partition of unity
3D high-order NMM
Derivative degrees of freedom
Continuous star-point stress

ABSTRACT

A three-dimensional (3D) high-order numerical manifold method (NMM) is developed based on the partition of unity method (PUM). We enrich the high-order NMM by introducing the derivative degrees of freedom associated with explicit physical significance. The global displacement in the formulation is approximated by a second-order approximation for the local displacement in conjunction with a first-order weight function. This not only helps the high-order NMM effectively avoid the problem of linear dependence that is frequently encountered in the PUM, but also renders the stress or strain at the star points continuous for the high-order NMM without the necessity of further smoothing operation. The effectiveness and robustness of the proposed new high-order NMM are demonstrated by several typical examples. Future potential developments and applications of the method are discussed.

1. Introduction

The numerical manifold method (NMM) [1] has received increasing attention in a wide range of engineering research areas, including fracture mechanics [2–8], fluid dynamics [9,10], seepage flow [11,12], the fourth order problems [13], the functionally graded materials [14], and isogeometric analysis [15]. Typically based on the first-order partition of unity (PU) [16], the NMM has recently been extended to higher orders, including the second [17] and the third order [18] developments with the addition of mathematical patches (MP) to cover a manifold element (ME), and the higher-order extension in [19] based on raising the order of local approximation. The various formulations of high-order NMM commonly suffer a serious issue of linear dependence (LD) which may further cause the notorious rank deficiency (RD) issue of the global stiffness matrix. To address this, a new algorithm has been developed [20] and further extended [21] to predict the RD. A dual local approximation scheme has also been introduced [22], and some strategies have been suggested in [23] to suppress this phenomenon. More recently, a two-dimensional (2D) high-order NMM with derivative degrees of freedom has been proposed by the authors [24] which may help to avoid the issue of linear dependence. Other latest developments of NMM encompass extensions based on an explicit formulation [25] and involving of strain-rotation decomposition to resolve large deformation and large rotation issues [26–28].

While 2D simplifications may be applicable to a number of cases, most real engineering problems are three-dimensional (3D). And as the enhanced version of FEM, 3D extended finite element method (3D-XFEM) was developed [29]. 3D generalized finite element method (3D-GFEM) was also proposed for investigating some 3D structural mechanics problems [30]. In addition, 3D mesh-free method [31] has also achieved some certain progress. It is hence desirable a full 3D NMM could be developed for practical application. There are two major challenges related to the 3D extension from a 2D NMM. (1) Choice of mesh. It may seem to be straightforward to formulate the 3D NMM using 4-node tetrahedral meshes [32,33]. However, for a practical problem, regular tetrahedrons may not completely fill a 3D space. Hence, the tetrahedral meshes at domain boundaries have to be subdivided and replaced by refined tetrahedrons [34,35]. Other mesh type can also be used, for example, hexahedral meshes have recently been employed in developing a new augmented NMM with flat-top PU by He et al. [36], which helps to avoid the issue of linear dependence in the NMM. A fault-cutting algorithm based on hexahedral meshes has also been developed [37]. (2) Physical significance of the undetermined coefficients. In most 2D NMM, the undetermined coefficients, or so-called as generalized degrees of freedom (DOFs) that are associated with the basis of the local approximation, do not possess concrete physical meanings. A recent study [23] has borrowed the concept of DOFs used in discontinuous deformation analysis (DDA) [38,39] for improvements. Similar ideas have been further used for a high-order NMM [24].

* Corresponding author.
E-mail addresses: huofan@ust.hk, huofan_HKUST@163.com (H. Fan).

http://dx.doi.org/10.1016/j.enganabound.2017.07.010
Received 18 December 2016; Received in revised form 1 July 2017; Accepted 10 July 2017

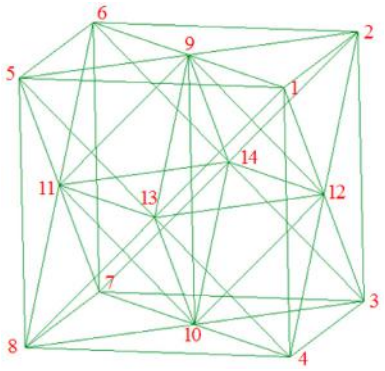

Twenty four tetrahedrons expressed by node number:

1: 1-12-4-13	9: 7-8-10-11	17: 9-11-13-5
2: 1-13-5-9	10: 5-8-11-13	18: 9-14-11-6
3: 1-2-12-9	11: 4-10-8-13	19: 10-11-14-7
4: 2-3-12-14	12: 3-4-12-10	20: 10-13-11-8
5: 2-9-6-14	13: 9-13-12-1	21: 11-13-14-9
6: 5-6-9-11	14: 9-12-14-2	22: 12-14-13-9
7: 6-7-14-11	15: 10-14-12-3	23: 11-14-13-10

Fig. 1. A hexahedron composed by 24 tetrahedrons.

This study aims at developing a high-order 3D NMM based on the tetrahedral meshes. A new local approximation is proposed to construct the global approximation based on the principle of PU. The DOFs with attributed physical meaning are incorporated into the high-order 3D-NMM, and its linear independence is verified by counting the number of zero eigenvalues of the global stiffness matrix [40,41]. The new local approximation for the 3D-NMM leads to a continuous stress field at the star point, hence avoiding the necessity of extra smoothing operation on the stress field.

2. Brief introduction of the NMM

In a 3D space, an arbitrary shape of problem domain can be filled by a mesh of hexahedrons. Each hexahedral element may be further subdivided into a number of tetrahedrons. Fig. 1 shows a hexahedron consisting of 24 tetrahedrons. A problem domain is referred to as the physical cover (PC) in the NMM. Fig. 2 shows a PC outlined by the black solid line with 120 tetrahedrons marked by the gray dotted line wherein we will focus on the specific tetrahedron manifold element (ME) 1234 highlighted by the red solid line. In the tetrahedral mesh, all tetrahedrons share the same node form a mathematical patch (MP) and the communal node is called the star. All these MPs forms a collective named mathematical cover (MC). It should be pointed out that the MPs can be an arbitrary geometry polyhedron, sphere, and ellipsoid, and among others. In Fig. 2, each MP is a polyhedron, see, *e.g.*, MP_1, MP_2, MP_3, and MP_4 associated with the tetrahedron 1234. Cutting the PC with the MPs generates the physical patches (PPs). For instance, MP_1, MP_2, MP_3, and MP_4 are cut by the resolution domain to form PP_1, PP_2, PP_3, and PP_4. The intersection of these four PPs then creates the ME 1234, as shown in Fig. 3. It is postulated that the global approximation defined over every ME is related to its correspounding 4 PPs. One can refer to Refs. [1,6,23,42] for more detailed formulation and description of the NMM.

3. Local and global approximation

The constant, ordinary power or trigonometric series can serve as the basis of function of NMM's local displacement approximation defined over each PP. If the power series is employed, for the kth PP it reads

$$\mathbf{u}_k(x,y,z)=\begin{Bmatrix}u_k(x,y,z)\\ v_k(x,y,z)\\ w_k(x,y,z)\end{Bmatrix}=\sum_{j=1}^{m}\begin{pmatrix}b_{kj}(x,y,z) & 0 & 0\\ 0 & b_{kj}(x,y,z) & 0\\ 0 & 0 & b_{kj}(x,y,z)\end{pmatrix}\begin{pmatrix}d_{k3j-2}\\ d_{k3j-1}\\ d_{k3j}\end{pmatrix} \tag{1}$$

where $b_{k,j}(x,y,z)$ is the basis function of a local displacement approximation and m is the number of $b_{k,j}(x,y,z)$. Assume that the number of PPs is n, and there are $3m$ unknowns in each PP, namely

$$D_k=\begin{pmatrix}d_{k1}\\ d_{k2}\\ \cdots\\ d_{k3m-2}\\ d_{k3m}\end{pmatrix},\ k=1,2,\ldots,n \tag{2}$$

where D_k is a basic unknown coefficient vector and has no apparent physical meaning, being referred to as generalized degrees of freedom. Nevertheless, the degrees of freedom of 2D-DDA have been endowed with the physical meaning and have been used to construct the local displacement approximation of NMM [24]. Following the core idea of Ref. [24], in this study, we will adopt the degrees of freedom of 3D-DDA [43] to establish the local approximation. Namely, Eq. (1) can be rewritten as

$$\mathbf{u}_k=\mathrm{T}^k\mathbf{d}_k \tag{3}$$

where

$$\mathbf{T}^k=\begin{bmatrix}N_k & 0 & 0 & N_{kx} & 0 & 0 & 0 & \frac{N_{kz}}{2} & \frac{N_{ky}}{2} & 0 & N_{kz} & -N_{ky}\\ 0 & N_k & 0 & 0 & N_{ky} & 0 & \frac{N_{kz}}{2} & 0 & \frac{N_{kx}}{2} & -N_{kz} & 0 & N_{kx}\\ 0 & 0 & N_k & 0 & 0 & N_{kz} & \frac{N_{ky}}{2} & \frac{N_{kx}}{2} & 0 & N_{ky} & -N_{kx} & 0\end{bmatrix} \tag{4}$$

and

$$\mathbf{d}_k=\left\{u^k\quad v^k\quad w^k\quad \varepsilon_x^k\quad \varepsilon_y^k\quad \varepsilon_z^k\quad \gamma_{yz}^k\quad \gamma_{zx}^k\quad \gamma_{xy}^k\quad \omega_x^k\quad \omega_y^k\quad \omega_z^k\right\}^{\mathrm{T}} \tag{5}$$

where ε_x^k, ε_y^k, ε_z^k, γ_{yz}^k, and γ_{xy}^k are the strain components at star (x_k,y_k,z_k). Moreover, ω_x^k, ω_y^k, and ω_z^k are the rotational angle of any infinitesimal vector passing the same star around the x-, y- and z-axis, respectively. Apparently, the basic unknown vector, $\mathbf{d}_k$, has clear physical meanings. In conjunction with Eqs. (4) and (5), after some mathematical manipulations, Eq. (3) can be rewritten as

$$\begin{aligned}\mathbf{u}_k(x,y,z)&=\begin{Bmatrix}u_k(x,y,z)\\ v_k(x,y,z)\\ w_k(x,y,z)\end{Bmatrix}\\ &=\begin{pmatrix}N_k u^k+N_{kx}\varepsilon_x^k+\frac{N_{kz}}{2}\gamma_{zx}^k+\frac{N_{ky}}{2}\gamma_{xy}^k+N_{kz}\omega_y^k-N_{ky}\omega_z^k\\ N_k v^k+N_{ky}\varepsilon_y^k+\frac{N_{kz}}{2}\gamma_{yz}^k+\frac{N_{kx}}{2}\gamma_{xy}^k-N_{kz}\omega_y^k+N_{kx}\omega_z^k\\ N_k w^k+N_{kz}\varepsilon_z^k+\frac{N_{ky}}{2}\gamma_{yz}^k+\frac{N_{kx}}{2}\gamma_{zx}^k+N_{ky}\omega_x^k-N_{kx}\omega_y^k\end{pmatrix}\end{aligned} \tag{6}$$

The shape functions defined on a tetrahedral mesh *ijmn* (see Fig. 4) is introduced

$$L_k=\frac{\tilde{a}_k+\tilde{b}_k x+\tilde{c}_k y+\tilde{d}_k z}{6V}=a_k+b_k x+c_k y+d_k z,\ k=i,j,m,n \tag{7}$$

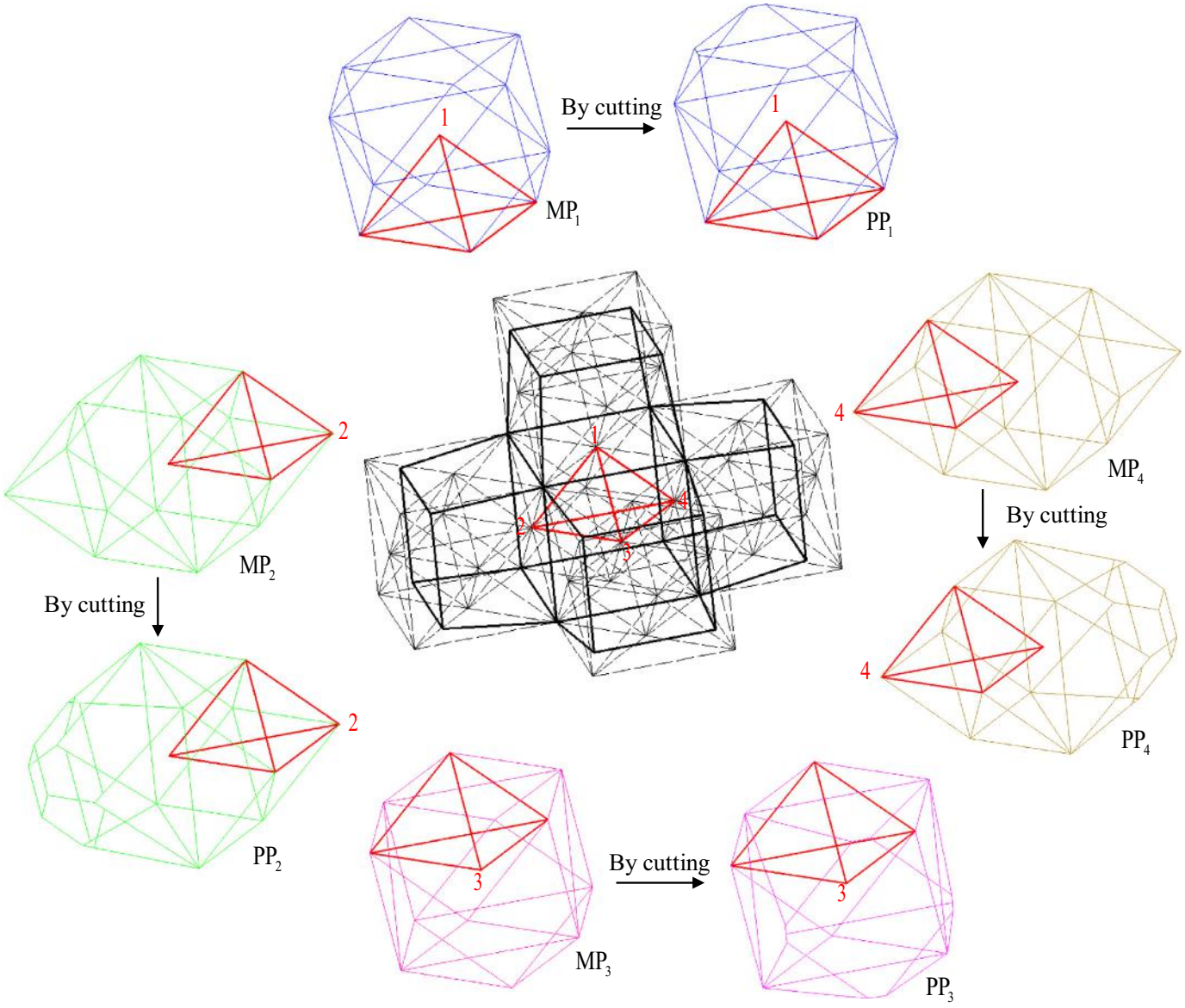

Fig. 2. PC, MC, MPs, and PPs of NMM.

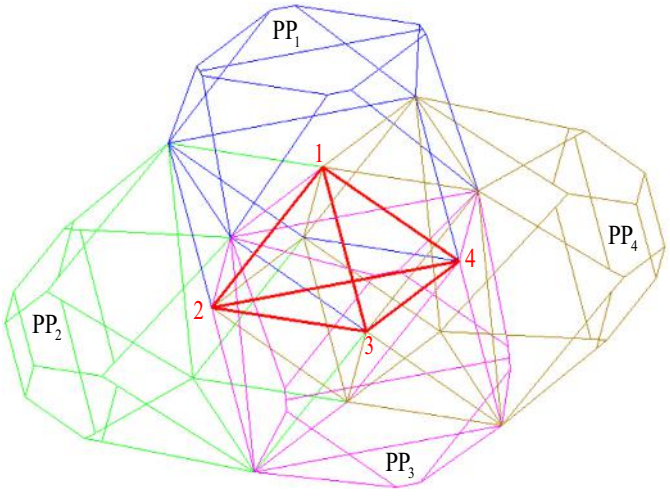

Fig. 3. A ME 1234 originated from PP_1, PP_2, PP_3, and PP_4.

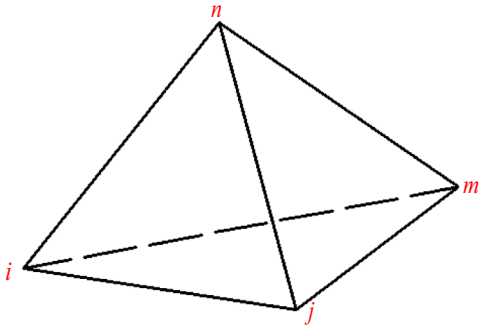

Fig. 4. A tetrahedral mesh *ijmn*.

where

$$6V = \det\begin{bmatrix} 1 & x_i & y_i & z_i \\ 1 & x_j & y_j & z_j \\ 1 & x_m & y_m & z_m \\ 1 & x_n & y_n & z_n \end{bmatrix} \tag{8}$$

Incidentally, V represents the volume of the tetrahedron. Further, we have

$$\tilde{a}_i = \det\begin{bmatrix} x_j & y_j & z_j \\ x_m & y_m & z_m \\ x_n & y_n & z_n \end{bmatrix},\ \tilde{b}_i = -\det\begin{bmatrix} 1 & y_j & z_j \\ 1 & y_m & z_m \\ 1 & y_n & z_n \end{bmatrix}$$
$$\tilde{c}_i = -\det\begin{bmatrix} x_j & 1 & z_j \\ x_m & 1 & z_m \\ x_n & 1 & z_n \end{bmatrix},\ \tilde{d}_i = -\det\begin{bmatrix} x_j & y_j & 1 \\ x_m & y_m & 1 \\ x_n & y_n & 1 \end{bmatrix} \tag{9}$$

with the other constants defined by cyclic interchange of the subscripts in the order of i, j, m, and n. For more details, one can refer to [44]. With these constants, we can define the variables in Eq. (4) as follows:

$$N_k = 3L_k - 2L_k^2 + 2\sum_{l\neq k} L_l L_k,\ l,k = i,j,m,n \tag{10}$$

and

$$\begin{aligned} N_{kx} &= \hat{a}_{in}\hat{N}_{kx} + \hat{a}_{jn}\hat{N}_{ky} + \hat{a}_{mn}\hat{N}_{kz} \\ N_{ky} &= \hat{b}_{in}\hat{N}_{kx} + \hat{b}_{jn}\hat{N}_{ky} + \hat{b}_{mn}\hat{N}_{kz},\ k = i,j,m,n \\ N_{kz} &= \hat{c}_{in}\hat{N}_{kx} + \hat{c}_{jn}\hat{N}_{ky} + \hat{c}_{mn}\hat{N}_{kz} \end{aligned} \tag{11}$$

where

$$\hat{a}_{kn} = x_k - x_n, \hat{b}_{kn} = y_k - y_n, \hat{c}_{kn} = z_k - z_n\ k = i,j,m \tag{12}$$

Here, (x_i,y_i,z_i), (x_j,y_j,z_j), (x_m,y_m,z_m), and (x_n,y_n,z_n) are the four "star" of the tetrahedral mesh covering one manifold element. Moreover,

$$\begin{aligned} \hat{N}_{ix} &= L_i(L_i-1) - (L_jL_m + L_mL_n + L_nL_j) \\ \hat{N}_{jx} &= L_i\left[L_j + 0.5(L_m+L_n)\right] \\ \hat{N}_{mx} &= L_i\left[L_m + 0.5(L_n+L_j)\right] \\ \hat{N}_{nx} &= L_i\left[L_n + 0.5(L_j+L_m)\right] \end{aligned} \tag{13}$$

additionally,

$$\begin{aligned} \hat{N}_{iy} &= L_j\left[L_i + 0.5(L_m+L_n)\right] \\ \hat{N}_{jy} &= L_j(L_j-1) - (L_mL_i + L_iL_n + L_nL_m) \\ \hat{N}_{my} &= L_j\left[L_m + 0.5(L_n+L_i)\right] \\ \hat{N}_{ny} &= L_j\left[L_n + 0.5(L_i+L_m)\right] \end{aligned} \tag{14}$$

and

$$\begin{aligned} \hat{N}_{iz} &= L_m\left[L_i + 0.5(L_j+L_n)\right] \\ \hat{N}_{jz} &= L_m\left[L_j + 0.5(L_n+L_i)\right] \\ \hat{N}_{mz} &= L_m(L_m-1) - (L_iL_j + L_jL_n + L_nL_i) \\ \hat{N}_{nz} &= L_m\left[L_n + 0.5(L_i+L_j)\right] \end{aligned} \tag{15}$$

Taking the shape function as the PU leads to

$$\phi_i = L_i,\ \phi_j = L_j,\ \phi_m = L_m,\ \phi_n = L_n \tag{16}$$

and $\varphi_k(k=i,j,m,n)$ can be written as

$$\begin{pmatrix} \phi_i \\ \phi_j \\ \phi_m \\ \phi_n \end{pmatrix} = \begin{pmatrix} f_{ii} & f_{ij} & f_{im} & f_{in} \\ f_{ji} & f_{jj} & f_{jm} & f_{jn} \\ f_{mi} & f_{mj} & f_{mm} & f_{mn} \\ f_{ni} & f_{nj} & f_{nm} & f_{mm} \end{pmatrix} \begin{pmatrix} 1 \\ x \\ y \\ z \end{pmatrix} \tag{17}$$

where $f_{lk}(l,k=i,j,m,n)$ are constants with respect to x_k, y_k, z_k $(l,k=i,j,m,n)$. By following the partition of unity method, the global displacement approximation defined over each manifold element can be expressed as

$$\begin{aligned} \mathbf{u}(x,y,z) &= \sum\nolimits_{k=i,j,m,n} \phi_k(x,y,z)\mathbf{u}_k(x,y,z) \\ &= \sum\nolimits_{k=i,j,m,n} \phi_k(x,y,z)\mathrm{T}^k\mathbf{d}_k = \sum\nolimits_{k=i,j,m,n} \bar{\mathrm{T}}^k\mathbf{d}_k \end{aligned} \tag{18}$$

where the interpolation function matrix is given by

$$\bar{\mathbf{T}}^k = \begin{bmatrix} \bar{N}_k & 0 & 0 & \bar{N}_{kx} & 0 & 0 & 0 & \frac{\bar{N}_{kz}}{2} & \frac{\bar{N}_{ky}}{2} & 0 & \bar{N}_{kz} & -\bar{N}_{ky} \\ 0 & \bar{N}_k & 0 & 0 & \bar{N}_{ky} & 0 & \frac{\bar{N}_{kz}}{2} & 0 & \frac{\bar{N}_{kx}}{2} & -\bar{N}_{kz} & 0 & \bar{N}_{kx} \\ 0 & 0 & \bar{N}_k & 0 & 0 & \bar{N}_{kz} & \frac{\bar{N}_{ky}}{2} & \frac{\bar{N}_{kx}}{2} & 0 & \bar{N}_{ky} & -\bar{N}_{kx} & 0 \end{bmatrix} \tag{19}$$

and

$$\bar{N}_k = \phi_k N_k,\ \bar{N}_{kx} = \phi_k N_{kx},\ \bar{N}_{ky} = \phi_k N_{ky},\ \bar{N}_{kz} = \phi_k N_{kz} \tag{20}$$

In Eqs. (19) and (20), $k = i, j, m, n$. Apparently, $\mathbf{u}(x,y,z)$ are three cubic polynomials defined on a 3D space.

The global displacement approximation possesses two observable properties:

(i). Alternate Kronecker-delta property

Due to the Kronecker-delta property of $\varphi_k(x,y,z)$, for $\bar{N}_k$,$\bar{N}_{kx}$,$\bar{N}_{ky}$, and $\bar{N}_{kz}$ the following equations hold:

$$\begin{aligned} \bar{N}_k(x_l,y_l,z_l) &= \delta_{kl},\ \frac{\partial \bar{N}_k(x_l,y_l,z_l)}{\partial x} = 0,\ \frac{\partial \bar{N}_k(x_l,y_l,z_l)}{\partial y} \\ &= 0,\ \frac{\partial \bar{N}_k(x_l,y_l,z_l)}{\partial z} = 0 \\ \bar{N}_{kx}(x_l,y_l,z_l) &= 0,\ \frac{\partial \bar{N}_{kx}(x_l,y_l,z_l)}{\partial x} = \delta_{kl},\ \frac{\partial \bar{N}_{kx}(x_l,y_l,z_l)}{\partial y} \\ &= 0,\ \frac{\partial \bar{N}_{kx}(x_l,y_l,z_l)}{\partial z} = 0 \\ \bar{N}_{ky}(x_l,y_l,z_l) &= 0,\ \frac{\partial \bar{N}_{ky}(x_l,y_l,z_l)}{\partial x} = 0,\ \frac{\partial \bar{N}_{ky}(x_l,y_l,z_l)}{\partial y} \\ &= \delta_{kl},\ \frac{\partial \bar{N}_{ky}(x_l,y_l,z_l)}{\partial z} = 0 \\ \bar{N}_{kz}(x_l,y_l,z_l) &= 0,\ \frac{\partial \bar{N}_{kz}(x_l,y_l,z_l)}{\partial x} = 0,\ \frac{\partial \bar{N}_{kz}(x_l,y_l,z_l)}{\partial y} \\ &= 0,\ \frac{\partial \bar{N}_{kz}(x_l,y_l,z_l)}{\partial z} = \delta_{kl} \end{aligned} \tag{21}$$

where k,l traverse i, j, m, n, and Eq. (21) is referred to as an alternate Kronecker-delta property of $\bar{N}_k$,$\bar{N}_{kx}$,$\bar{N}_{ky}$, and $\bar{N}_{kz}$

(ii) $\mathbf{u}$ (x, y, z) is C^1 at the star points.

On the other hand, the global displacement approximation can be expressed as

$$\mathbf{u}(x,y,z) = \bar{\mathbf{T}}^i\mathbf{d}_i + \bar{\mathbf{T}}^j\mathbf{d}_j + \bar{\mathbf{T}}^m\mathbf{d}_m + \bar{\mathbf{T}}^n\mathbf{d}_n \tag{22}$$

Further, we can easily obtain the derivative of $\mathbf{u}(x, y, z)$ as

$$\begin{aligned} \mathbf{u}_{,x}(x,y,z) &= \bar{\mathbf{T}}^i_{,x}\mathbf{d}_i + \bar{\mathbf{T}}^j_{,x}\mathbf{d}_j + \bar{\mathbf{T}}^m_{,x}\mathbf{d}_m + \bar{\mathbf{T}}^n_{,x}\mathbf{d}_n \\ \mathbf{u}_{,y}(x,y,z) &= \bar{\mathbf{T}}^i_{,y}\mathbf{d}_i + \bar{\mathbf{T}}^j_{,y}\mathbf{d}_j + \bar{\mathbf{T}}^m_{,y}\mathbf{d}_m + \bar{\mathbf{T}}^n_{,y}\mathbf{d}_n \\ \mathbf{u}_{,z}(x,y,z) &= \bar{\mathbf{T}}^i_{,z}\mathbf{d}_i + \bar{\mathbf{T}}^j_{,z}\mathbf{d}_j + \bar{\mathbf{T}}^m_{,z}\mathbf{d}_m + \bar{\mathbf{T}}^n_{,z}\mathbf{d}_n \end{aligned} \tag{23}$$

Considering property (i) results in the following equalities

$$\mathbf{u}_{,x}(x_k,y_k,z_k) = \mathbf{u}_{k,x}(x_k,y_k,z_k) = \begin{pmatrix} \varepsilon_x^k \\ \frac{1}{2}\gamma_{xy}^k + \omega_z^k \\ \frac{1}{2}\gamma_{zx}^k - \omega_y^k \end{pmatrix} \tag{24}$$

$$\mathbf{u}_{,y}(x_k,y_k,z_k) = \mathbf{u}_{k,y}(x_k,y_k,z_k) = \begin{pmatrix} \frac{1}{2}\gamma_{xy}^k - \omega_z^k \\ \varepsilon_y^k \\ \frac{1}{2}\gamma_{yz}^k + \omega_x^k \end{pmatrix} \tag{25}$$

$$\mathbf{u}_{,z}(x_k,y_k,z_k) = \mathbf{u}_{k,z}(x_k,y_k,z_k) = \begin{pmatrix} \frac{1}{2}\gamma_{zx}^k + \omega_y^k \\ \frac{1}{2}\gamma_{yz}^k - \omega_x^k \\ \varepsilon_z^k \end{pmatrix} \tag{26}$$

Therefore, we can conclude that $\mathbf{u}(x, y, z)$ is C^1 continuous at the star, namely, the stress values of star are continuous and there is no need for smoothing operations.

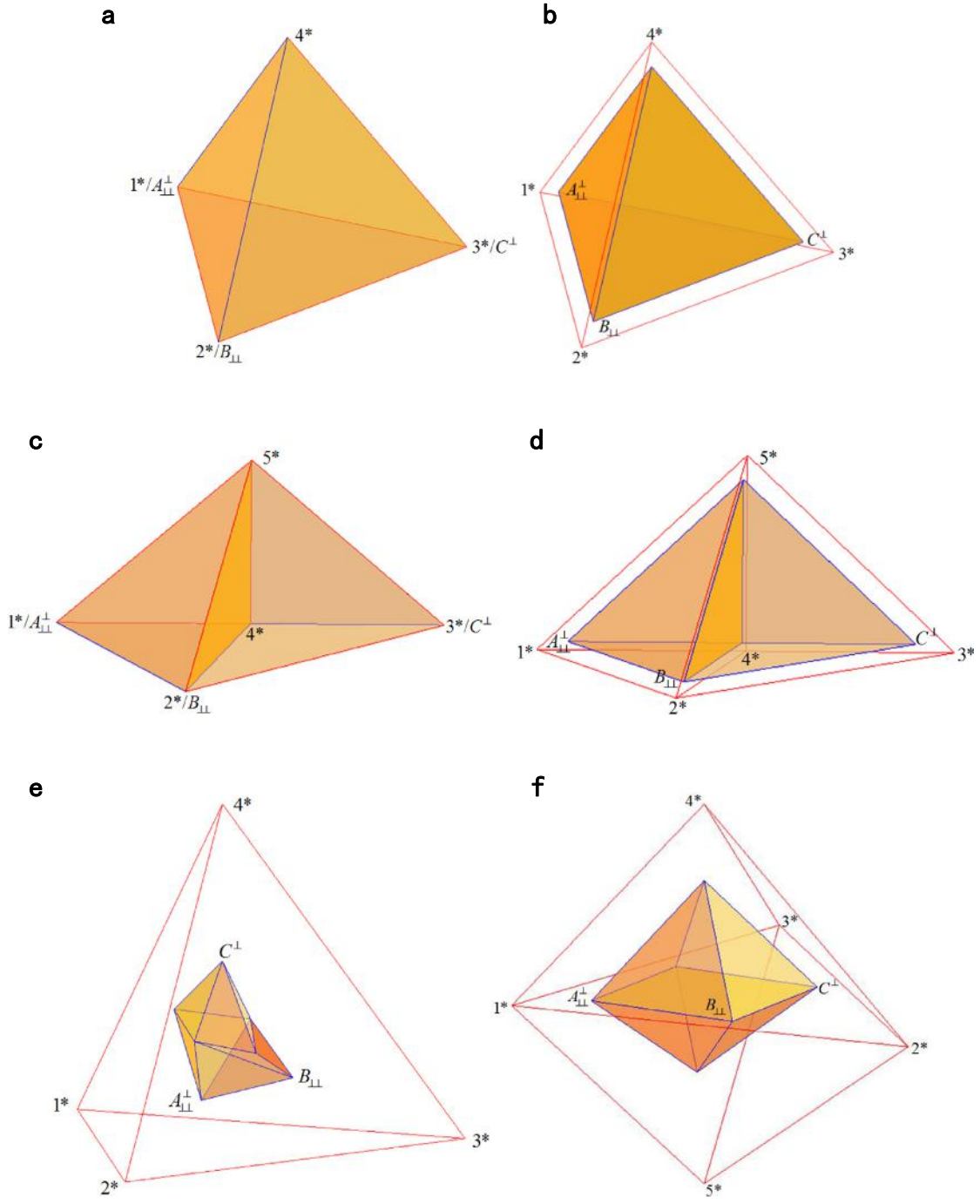

Fig. 5. Configurations for eigenvalue analysis. (a) a TME a TMM; (b) a TME a TMM; (c) two TMEs two TMMs; (d) two TMEs two TMMs; (e) a IME a TMM; and (f) two PMEs two TMMs.

4. Simultaneous equations

For a problem domain Ω with the essential boundary Γ_u and the natural boundary Γ_t, using the variational principle [45], we have the following weak form

$$\int_{\Omega} \boldsymbol{\sigma} : \delta\boldsymbol{\varepsilon} d\Omega - \int_{\Omega} \mathbf{b}\cdot\delta\mathbf{u} d\Omega - \int_{\Gamma_t} \bar{\mathbf{t}} : \delta\mathbf{u} d\Gamma + \int_{\Gamma_u} \mathbf{k}(\mathbf{u}-\bar{\mathbf{u}})\cdot\delta\mathbf{u} d\Gamma = 0 \qquad (27)$$

where $\boldsymbol{\sigma}$ and $\boldsymbol{\varepsilon}$ are the Cauchy stress and strain vector, respectively. $\mathbf{b}$ is the unit body force vector, and $\bar{\mathbf{t}}$ and $\bar{\mathbf{u}}$ the prescribed traction on the natural boundary and the prescribed displacement on the essential boundary, respectively. The reason for containing the last term in Eq. (27) is because the mathematical cover system is not necessarily consistent with the boundaries in NMM and because the above-mentioned alternate Kronecker-delta property in the last section only ensures the correct essential boundary conditions at stars or nodes. And the penalty

Table 1
Results for eigenvalue analysis, see Fig. 5.

Configuration	Total Dofs	Before applying constrains: Number of zero eigenvalues	After applying constrains: Number of zero eigenvalues
(a)	48	6	0
(b)	48	6	0
(c)	60	6	0
(d)	60	6	0
(e)	48	6	0
(f)	60	6	0

matrix **k** is given by

$$\mathbf{k} = \begin{bmatrix} k_x & & \\ & k_y & \\ & & k_z \end{bmatrix} \tag{28}$$

where k_x, k_y, and k_z are the penalty numbers of the x-, y-, and z-axis directions, respectively. The substitution of Eq. (22) into Eq. (27) yields

$$\mathbf{Kd} = \mathbf{F} \tag{29}$$

where **K** is the global equivalent stiffness matrix, **d** is the global basic unknown vector, and **F** is the global equivalent loading vector. In general, **K** contains inertia matrix, fixed point matrix, contact matrix, and so on. While **F** includes initial stress vector, point loading vector, body loading vector, contact force vector, and friction vector. Their assembling process is similar to finite element method and one can refer to Refs. [1, 18] for more details.

The Appendix I summarizes the computation of the stiffness matrix of element, and this procedure can be applied to the other sub-matrixes and can be extended to any 3D low- or high-order NMM based on the tetrahedral mesh.

5. Numerical examples

In this section, the used physical units are based on the international standard unit system, unless stated otherwise. And, the relative L^2 error in the energy norm [44] is adopted to estimate the accuracy and convergence, it is defined by

$$e = \frac{\sqrt{\int_\Omega (\boldsymbol{\varepsilon}^{\mathrm{Ref}} - \boldsymbol{\varepsilon}^{\mathrm{Cal}})^{\mathrm{T}} \mathbf{D} (\boldsymbol{\varepsilon}^{\mathrm{Ref}} - \boldsymbol{\varepsilon}^{\mathrm{Cal}})}}{\sqrt{\int_\Omega (\boldsymbol{\varepsilon}^{\mathrm{Ref}})^{\mathrm{T}} \mathbf{D} \boldsymbol{\varepsilon}^{\mathrm{Ref}}}} \tag{30}$$

where the superscript "Ref" indicates the reference solution, and the superscript "Cal" represents the calculated value. Due to the lack of analytical solution for the examples 5.4 up to 5.7, the reference solution used here correspond to the discrete model with the maximum element numbers. And for calculating Eq. (30) the numerical integration has to be resorted. Here, the Keast integration rule [46,47] is employed. Moreover, the linear fitting is employed to obtain the convergence rates.

5.1. Eigenvalue analysis

The eigenvalue analysis [40,41] has been commonly used to test the linear independence of a PU-based method. It consists of two steps: (1) Without prescribing any boundary conditions, the eigenvalues of the global stiffness matrix can be determined first. In this step, it is possible that zero eigenvalues can be obtained. (2) By exerting a minimum number of constraints to limit rigid motions of the model, *i.e.*, applying 6 restricted conditions for a 3D case, re-calculate the eigenvalues of the global stiffness matrix. If only nonzero eigenvalues are found at this second step, it can be concluded that the method under investigation is frees from linear dependence problem.

Considering the mathematical mesh can be selected to match or not match with the problem domain in the NMM, and the simplex integration method [48] can be applied to an arbitrary polyhedron. In this test, six cases as shown in Fig. 5 are designed. A tetrahedron manifold element (TME) that coincides with a tetrahedron mathematical mesh (TMM) is shown in Fig. 5(a), while a TME and a slightly larger TMM are sketched in Fig. 5(b). Two cases can be identified involving two TMEs and two TMMs as illustrated in Fig. 5(c) and (d), respectively. Fig. 5(e) shows an irregular manifold element (IME) and a TMM. Moreover, two

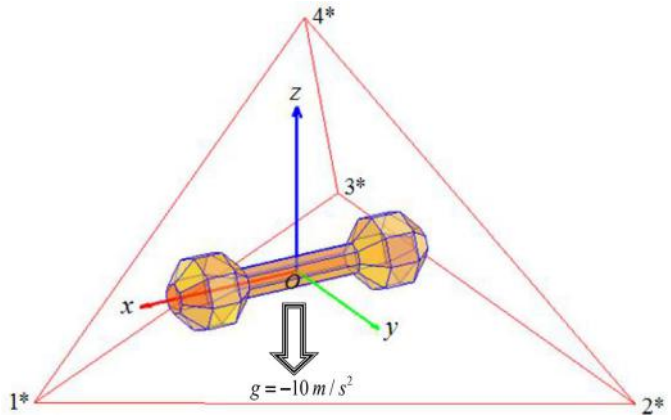

Fig. 6. Free falling of a dumbbell.

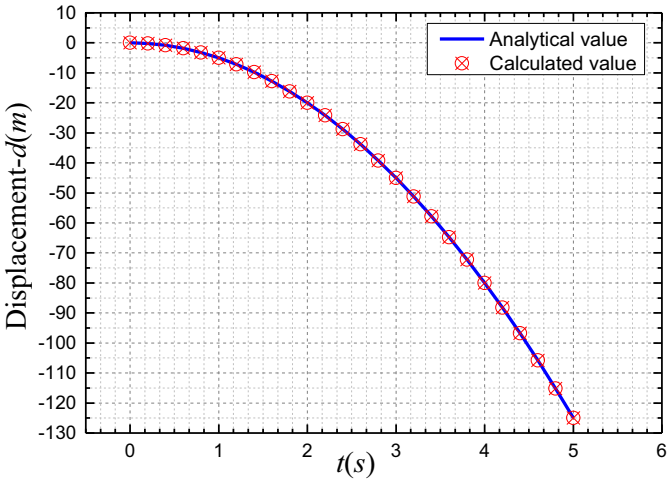

Fig. 7. Displacement-*d vs. t* of the centroid point O.

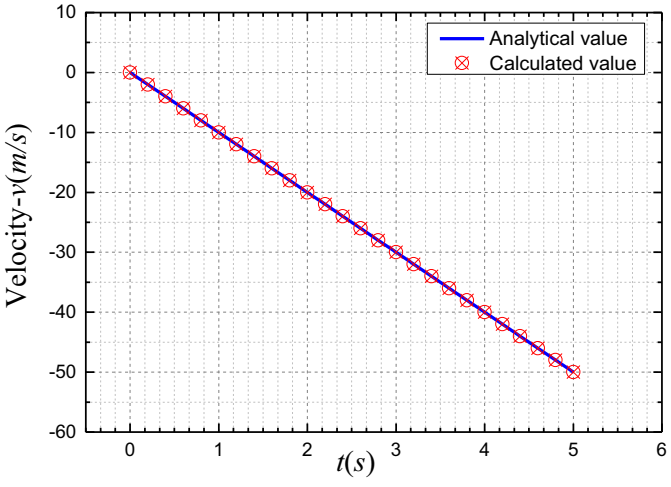

Fig. 8. Velocity-*v vs. t* of the centroid point O.

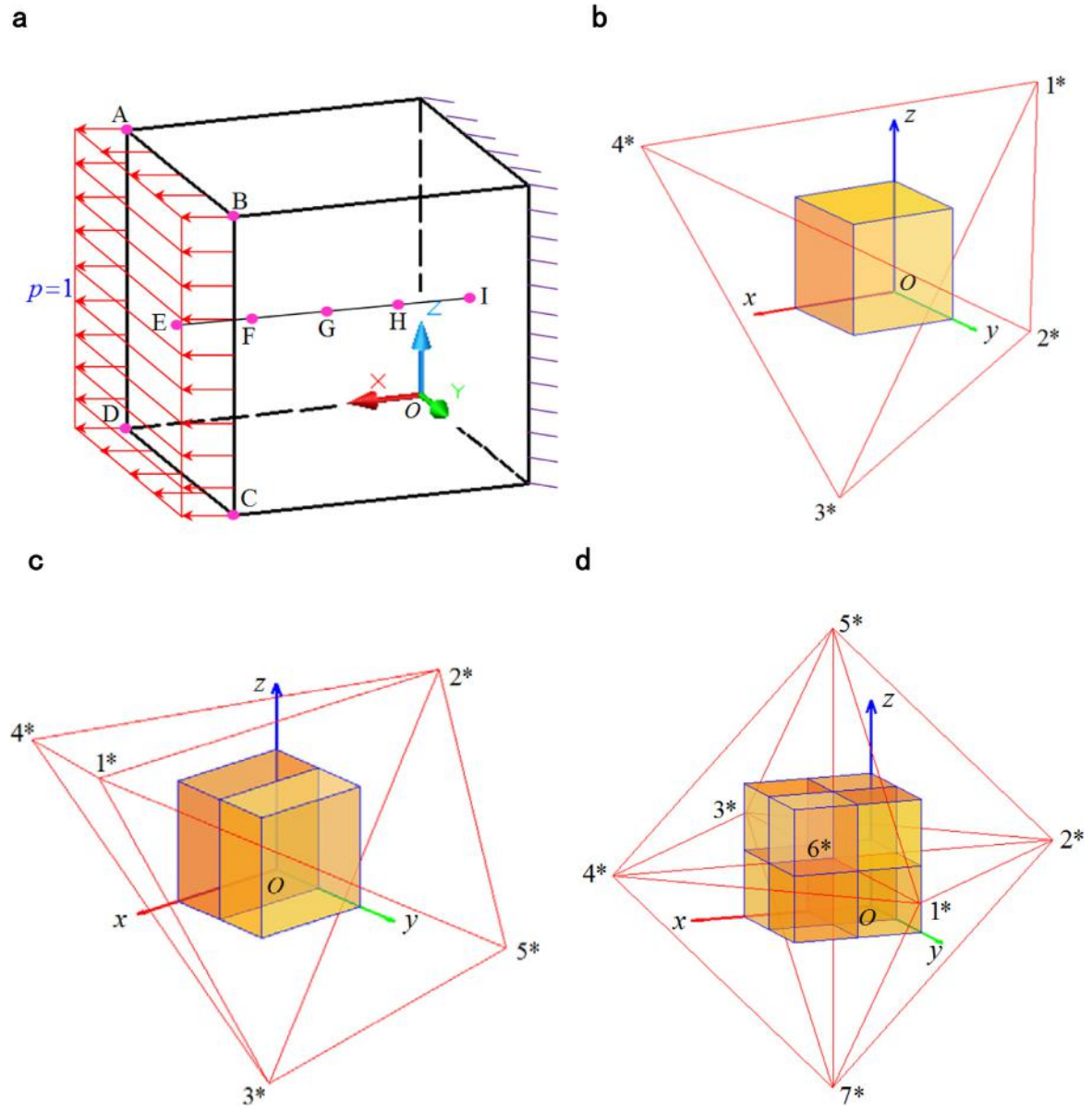

Fig. 9. Uniaxial tension of a cube. (a) Configuration; (b) one tetrahedron MC; (c) two tetrahedron MC and (d) eight tetrahedron MC. (For interpretation of the references to color in this figure legend, the reader is referred to the web version of this article.)

Table 2
Results for the uniaxial tension of a cube, see Fig. 9.

CP	Coordinate	Displacement Calculated value	Reference value
A	(1.0, 0.0, 1.0)	0.000001000000011	0.000001
B	(1.0, 1.0, 1.0)	0.000001000000011	0.000001
C	(1.0, 1.0, 0.0)	0.000001000000011	0.000001
D	(1.0, 0.0, 0.0)	0.000001000000011	0.000001
E	(1.0, 0.5, 0.5)	0.000001000000011	0.000001
F	(0.75, 0.5, 0.5)	0.000000750000013	0.00000075
G	(0.5, 0.5, 0.5)	0.000000500000012	0.0000005
H	(0.25, 0.5, 0.5)	0.000000250000013	0.00000025
I	(0.0, 0.5, 0.5)	0.000000000000010	0.0

CP: Checking point.

pentahedron manifold elements (PMEs) and two TMMs are also tested as shown in Fig. 5(f).

The material constants used for the analysis are the Young's modulus of $E = 1.0$ and Poisson's ratio of $\upsilon = 0.25$, and the gravity is ignored. The counts of computed zero eigenvalues are listed in Table 1. A total of six zero eigenvalues are found for all cases before applying any constrain (Step 1). When six constrains are applied for Step 2 analysis, no zero eigenvalues are observed. Thus, we conclude that the proposed method is free from the LD problem.

5.2. *Free falling of a dumbbell*

The first benchmark example for the proposed NMM is the free falling process of a dumbbell. A dumbbell is treated as an irregular element and covered by a tetrahedron $1^*2^*3^*4^*$, as shown in Fig. 6. The dumbbell falls under gravity only. The gravitational acceleration is given by $g = -10\,\mathrm{m/s^2}$, and the time step used is 0.1 s. Figs. 7 and 8 depict the displacement and velocity time history of the centroid point O of the dumbbell. For the displacement ($d = 0.5gt^2$), the absolute value of the relative error between the analytical values and the calculated values is less than 0.000004%, while for the velocity ($v = gt$), the corresponding absolute value is less than 0.000002%. It evidences that the high-order NMM may achieve rather excellent accuracy.

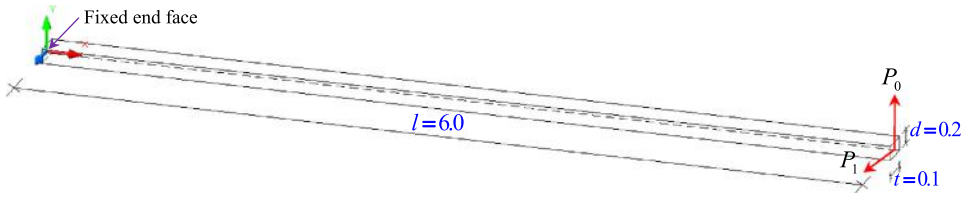

Fig. 10. A slender cantilever beam under point loading.

Table 3
Results for the deflection of loading point.

MEs	In-plane force P_0 1-order	Proposed	Out-of-plane P_1 1-order	Proposed
240	0.1144	0.9691	0.0537	0.9331
480	0.1628	0.9710	0.0466	0.9611
720	0.3062	0.9831	0.1002	0.9810
960	0.4422	0.9947	0.1672	0.9936
1200	0.5556	0.9951	0.2413	0.9941

Normalized by Ref. [49]: 0.1081 for P_0; 0.4321 for P_1. MEs: manifold elements.

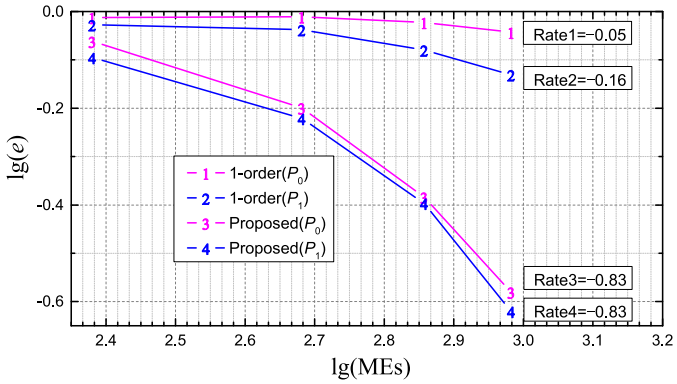

Fig. 11.. Relative error in energy norm for a slender cantilever beam.

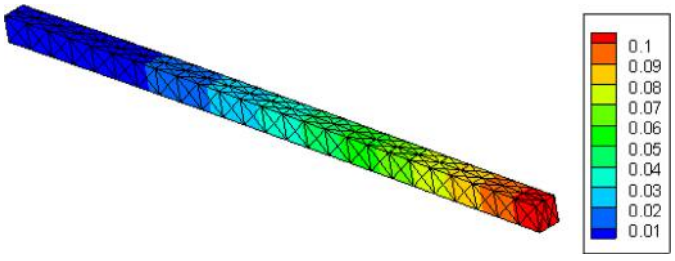

Fig. 12. Contour plot of the displacement for P_0 (1200 MEs).

5.3. Uniaxial tension of a cube

The uniaxial tension of a $1.0\times1.0\times1.0$ cube as shown in Fig. 9(a) is chosen as the second benchmark example, where a unit distributed load is applied to the left end-face and the right end-face is fixed. Points A to I marked by violet color in Fig. 9(a) serve as the nine checking points (CP). The chosen Young's modulus is set to be $E=1.0\times10^6$ and the gravity is not considered. Moreover, the Poisson's ratio is chosen as $\upsilon=0$, by doing so, an artificial uniaxial stressed state can be achieved. In this example, three types of MC are considered, *i.e.* one tetrahedron, two tetrahedrons, and eight tetrahedrons, as shown in Fig. 9(a), (b), and (c), respectively. For the three types of MC, our calculation indicates that the numerical values obtained by the high-order NMM are all in good agreement with the reference ones (see Table 2). The calculated values corresponding to the third type of MC (8 tetrahedrons) are summarized in Table 2 in comparison with the reference values. From Table 2, we

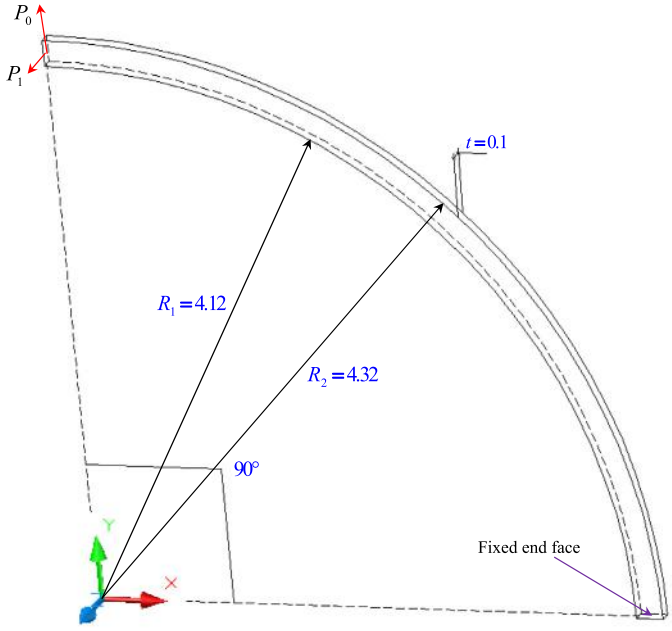

Fig. 13. A curved cantilever beam under point loading.

Table 4
Normalized displacement of loading point along the direction of loading.

MEs	In-plane force P_0 1-order	Proposed	Out-of-plane P_1 1-order	Proposed
480	0.2901	0.8749	0.1348	0.7676
720	0.4680	0.9353	0.2600	0.7895
960	0.5906	0.9539	0.3820	0.8561
1200	0.6665	0.9688	0.4812	0.9435
1440	0.7119	0.9871	0.5529	0.9794

Normalized by the reference solution [49]: 0.08734 for P_0; 0.5022 for P_1. MEs: manifold elements.
MEs: manifold elements.

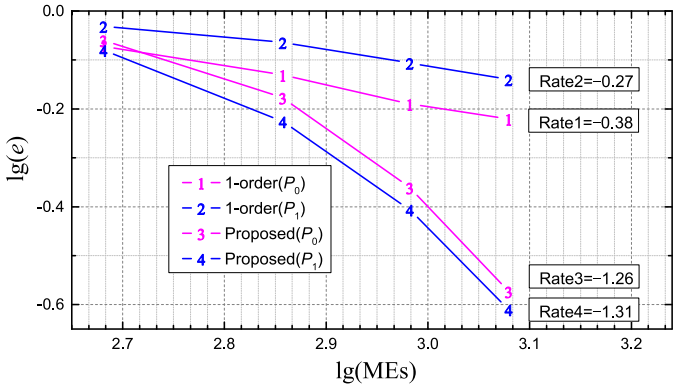

Fig. 14. Relative error in energy norm for a curved cantilever beam.

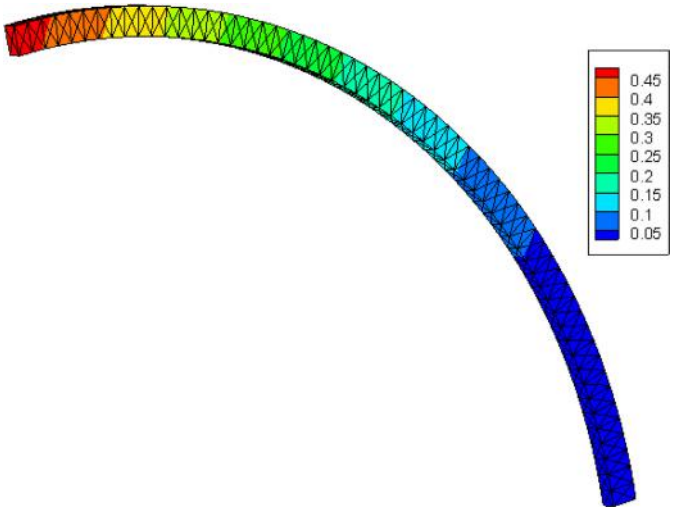

Fig. 15. Contour plot of the displacement for P_1 (1440 MEs).

Table 5
Displacement of point A in the direction of *y*-axis.

MEs	1-order	Proposed
216	0.3109	0.9676
384	0.4458	0.9842
600	0.5844	0.9898
864	0.6984	0.9924
1176	0.7812	0.9939

Normalized by the reference solution [50]: 23.96.

can see that the numerical solution given by the high-order NMM is almost identical to the reference one.

5.4. A slender cantilever beam under point loading

Shown in Fig. 10 is a third example of a slender cantilever beam with the length $l=6.0$, width $t=0.1$, and depth $d=0.2$ to benchmark

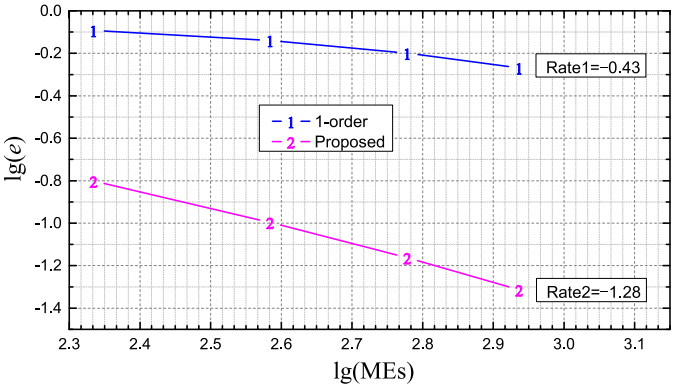

Fig. 17. Relative error in energy norm for Cook's beam.

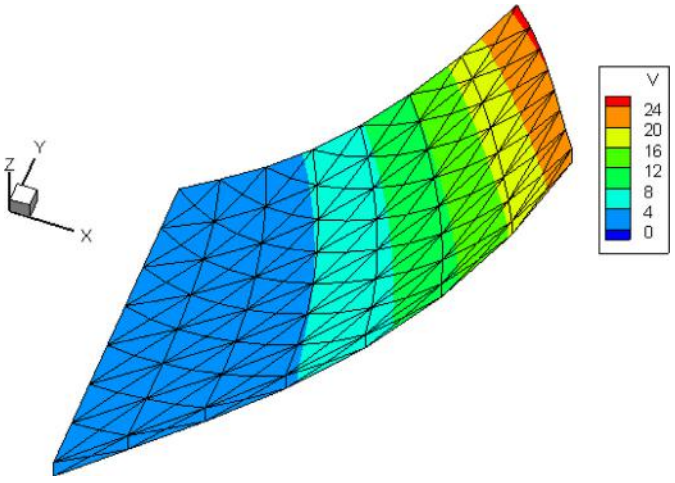

Fig. 18. Contour plot of the displacement in direction of *y*-axis (1176 MEs).

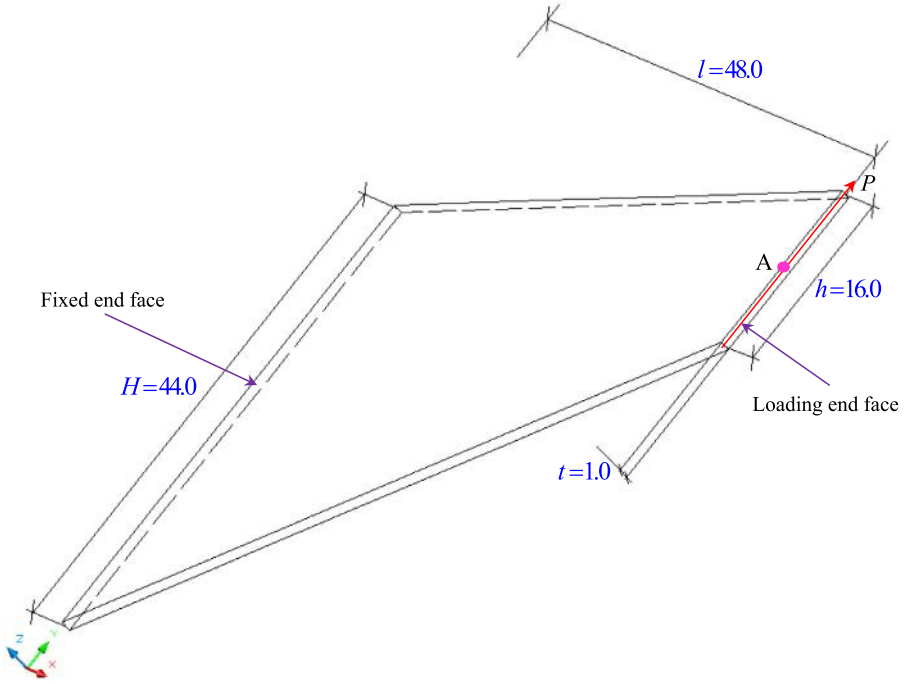

Fig. 16. Cook's beam under distributed load.

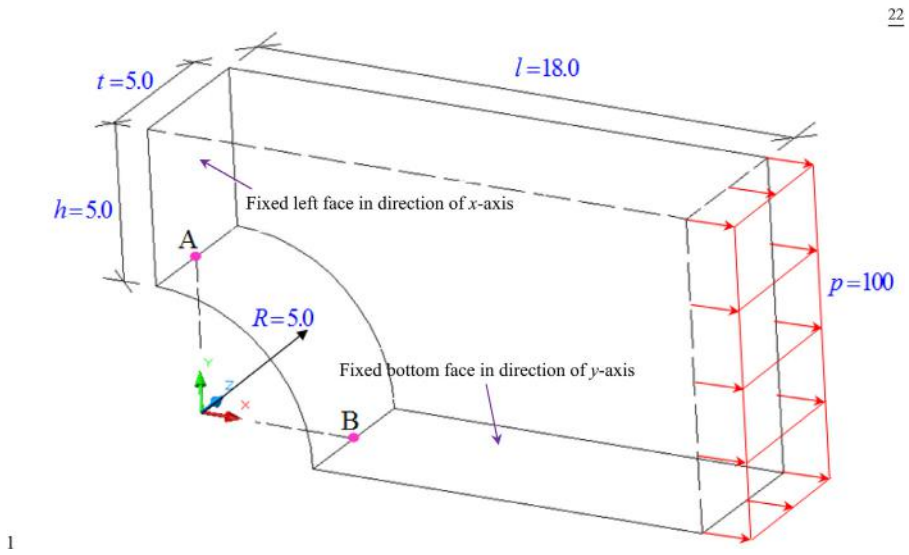

Fig. 19. Quarter geometry of a finite plate under tensile loading.

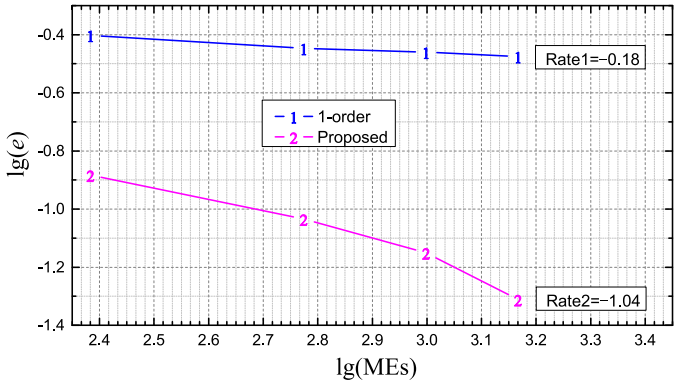

Fig. 20. Relative error in energy norm for Cook's beam.

the proposed NMM. The left end-face of the cantilever beam is fixed, and an in-plane force $P_0 = 1$ or an out-of-plane force $P_1 = 1$ is exerted on the center point of the free end. The Young's Modulus set to be $E = 1.0 \times 10^7$ and the Poisson's ratio is taken to be $\upsilon = 0.30$. To examine the trend of convergence of the numerical solution, we investigate several discrete models that include 240, 480, 720, 960, and 1200 MEs, respectively.

The numerical solutions are listed in Table 3 along with the corresponding reference solutions. For the proposed method, with the increase of element number used, the numerical results apparently converge to the reference solution. While for the conventional 1-order tetrahedron element, as MEs = 1200 the normalized values are only 0.5556 and 0.2413 corresponding to the force P_0 and P_1, respectively.

The curve of lg(*e*) *vs.* lg(MEs) is further sketched in Fig. 11. From this figure, we can see that the convergence rates of the proposed method are −0.83(for P_0 and P_1) comparing to the convergence rates −0.05(for P_0) and −0.16(for P_1) of the conventional 1-order tetrahedron element. In addition, Fig. 12 shows further the contour of the displacement corresponding 1200 MEs.

5.5. A curved cantilever beam under point loading

A further illustrative example is a curved or quadrant cantilever beam shown in Fig. 13, in which the inside radius R_1, outside radius R_2, and the thickness t are 4.12, 4.32, and 0.1, respectively. A unit in-plane P_0 or an out-of-plane force P_1 is applied on the center point of its free end face, respectively. The chosen Young's Modulus is $E = 1.0 \times 10^7$

Table 6
Normalized σ_{VM} of points A and B by reference values.

MEs	For point A 1-order	Proposed	For point B 1-order	Proposed
242	0.6096	0.8735	0.5942	0.7585
595	0.6990	0.9491	0.7366	0.9383
997	0.8251	0.9789	0.8093	0.9642
1469	0.8733	0.9843	0.8345	0.9886
2294	0.8936	0.9910	0.8778	0.9927

Normalized by the reference solution [51]: 442 for point A; 179 for point B.
MEs: manifold elements.

and Poisson's ratio $\upsilon = 0.25$. Several discrete models, *i.e.* 480, 720, 960, 1200, and 1440 MEs, are examined.

The numerical and reference solutions are summarized in Table 4. When MEs = 1440, the normalized displacement are equal to 0.7119(for P_0) and 0.5529 (for P_1) corresponding to the conventional 1-order tetrahedron element. While for the proposed method, the normalized values are equal to 0.9871(for P_0) and 0.9794 (for P_1).

The curve of lg(*e*) *vs.* lg(MEs) of this example is shown in Fig. 14. As we can see, the convergence rates of the proposed method are −1.26(for P_0) and −1.31(for P_1), which are much more than −0.38(for P_0) and −0.27(for P_1) corresponding to the conventional 1-order tetrahedron element. Moreover, for the case of 1440 MEs, the contours of the corresponding displacement are further exhibited in Fig. 15. As we can see, a good agreement with the analytical solutions can be obtained along with the increase of element number.

5.6. Cook's beam

Cook's skew beam problem [50] shown in Fig. 16 is further chosen for benchmarking the proposed NMM. The chosen heights H and h of the beam are 44.0 and 16.0, respectively; while length l and thickness t are 48.0 and 1.0, respectively. The left end face is fixed, and a uniformly distributed load with the total value of $P = 1.0$ acts on the right end face. The center point A (48.0, 44.0, 0.0) of the right end face are chosen as the checking point. The material constants Young's modulus of $E = 1.0$ and Poisson's ratio of $\upsilon = 1/3$, and the gravity is not considered. In this example, we will examine the displacement of the center point of the loading face. Similarly, a series of 216, 384, 600, 864, and 1176 MEs are examined. The numerical results are summarized in Table 5.

Table 5 indicates that the calculated displacement at Point A obtained by the present high-order NMM approaches to the reference value

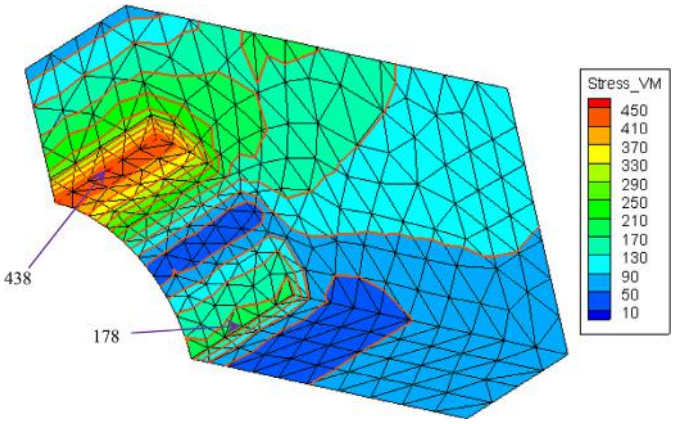

Fig. 21. Contour plot of σ_{VM} (2294 MEs).

(23.96) gradually. When MEs = 1176, the normalized values are equal to 0.7812 and 0.9939 corresponding to the conventional 1-order tetrahedron element and the presented method, respectively.

Fig. 17 show the curve of lg(*e*) *vs.* lg(MEs). The convergence rates of the conventional 1-order tetrahedron element and the proposed method are −0.43 and −1.28, respectively. For the case with 1176 MEs, the contour of the displacement in direction of *y*-axis illustrated in Fig. 18 also appears to be rather reasonable.

5.7. Finite plate with a central hole under tensile loading

A further example chosen for investigation is the quarter geometry of a finite plate with a central hole shown in Fig. 19, in which the length *l*, height *h*, and thickness *t* are 18.0, 5.0, and 5.0, respectively. The radius of the central hole is $R = 5.0$. The von Mises stress σ_{VM} at points A(0.0, 5.0, 0.0) and B(5.0, 0.0, 0.0) will be examined. The chosen material constants are Young's modulus of $E = 72.0 \times 10^9$ and Poisson's ratio of $\upsilon = 0$. A uniformly distributed load $p = 100$ is applied to the right end face, while the gravity is ignored. Due to the symmetry of the structure, the left and bottom end face are fixed in direction of *x*- and *y*-axis, respectively. In this example, a series of 242, 595, 997, 1469, and 2389 MEs are considered and the computed results are listed in Table 6.

With the increase of element number, Table 6 shows the calculated stress values by the proposed NMM converge gradually to the reference solution and is faster than the conventional 1-order tetrahedron element.

For this example, the curve of lg(*e*) *vs.* lg(MEs) is illustrated in Fig. 20. The convergence rates of the conventional 1-order tetrahedron element and the proposed method are −0.18 and −1.04, respectively. Additionally, the contour of von Mises stress corresponding to the case of 2294 MEs is shown in Fig. 21, which demonstrates an apparent continuity for the stress field. Hereby no smoothing operation is required.

6. Conclusions

A new 3D high-order NMM has been developed based on the principle of partition of unity. Key ingredients in the new NMM are the inclusion of generalized degrees of freedom pertaining to clear physical significance and new formulations on the local and global approximations function which renders the rid of linear dependence issue of the NMM. Due to the delta property of partition of unity functions, the proposed method leads to C^1 continuity for the global displacement approximation, and hence makes the strain or stress continuous at the star shared by several adjacent elements. This makes the smoothing operations for the stress field totally unnecessary. In addition, the used procedure for computing sub-matrix, which is indispensable for generating the governing equations of system, can be extended to any 3D low- or high-order NMM based on the tetrahedral mesh. In the future, the proposed high-order NMM will be applied to finite deformation and crack analysis.

Acknowledgments

This study is partially supported by the University Grants Council of Hong Kong through a Collaborative Research Fund (CRF) Project C6012-15G. This study is also supported by the National Basic Research Program of China (973 Program, Grant No. 2014CB047100); and the National Natural Science Foundation of China (Grant Nos. 11172313 and 51538001).

Appendix I

A procedure for calculating some sub-matrixes involving volume integral

For 4-node tetrahedral mesh, we have the following formula

$$f = L_i^a L_j^b L_m^c L_n^d \tag{A.1}$$

In this study, Eq. (A.1) is referred as "L_{ijmn}-monomial" . Assume that the highest order of f is 6, then there is the following constrains on Eq. (A.1)

$$\begin{cases} a, b, c, d = 1, 2, \ldots, 6 \\ 0 \le a + b + c + d \le 6 \end{cases} \tag{A.2}$$

Easily, one can obtain 210 L_{ijmn}-monomials, as follows

$$\begin{cases} f_1 = 1 \\ f_2 = L_i \\ f_3 = L_j \\ f_4 = L_m \\ f_5 = L_n \\ \quad \vdots \\ f_{210} = L_n^6 \end{cases} \tag{A.3}$$

Similarly, we have

$$g = x^a y^b z^c, \quad \begin{cases} a, b, c, d = 1, 2, \ldots, 6 \\ 0 \le a + b + c + d \le 6 \end{cases} \tag{A.4}$$

and

$$\begin{cases} g_1 = 1 \\ g_2 = x \\ g_3 = y \\ g_4 = z \\ g_5 = x^2 \\ \quad \vdots \\ g_{84} = z^6 \end{cases} \tag{A.5}$$

In this study, Eq. (A.4) is referred as "*xyz*-monomial" . For a 3D-simplex, we can save the simplex integration value of *xyz*-monomial into the following 3D array *S* (Fig. A1). Based on the 3D array *S*, we can directly extract the integration value of any *xyz*-monomial. Taking as $\int x^3 y^4 z^5 dv$ for an example, through the power-exponent we can access the corresponding value, namely,

$$S[3][4][5] = \int x^3 y^4 z^5 dv \tag{A.6}$$

Substituting Eq. (7) into Eq. (A.3) leads to

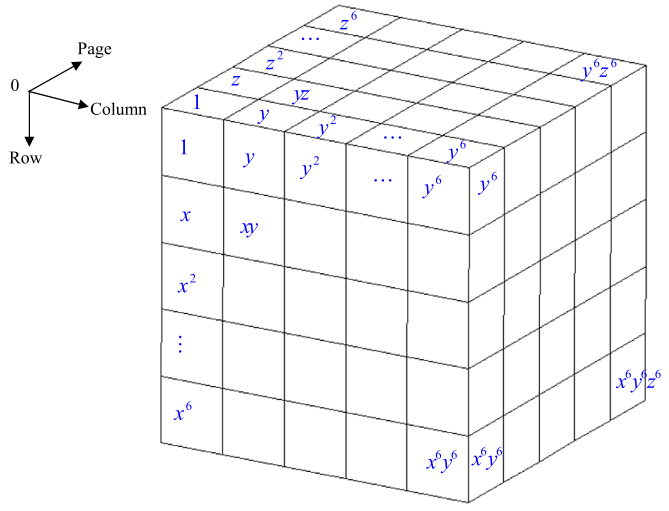

Fig. A1. Value of simplex integration of *xyz*-monomial in a 3D array.

$$\begin{cases} l_1 = 1 \\ l_2 = a_i + b_i x + c_i y + d_i z \\ l_3 = a_j + b_j x + c_j y + d_j z \\ l_4 = a_m + b_m x + c_m y + d_m z \\ l_5 = a_n + b_n x + c_n y + d_n z \\ \vdots \\ l_{210} = (a_n + b_n x + c_n y + d_n z)^6 \end{cases} \tag{A.7}$$

Expanding Eq. (A.7) and with the help of the 3D array S, we can calculate the following integration

$$\begin{cases} \int_e l_1 dv \\ \int_e l_2 dv \\ \vdots \\ \int_e l_{210} dv \end{cases} \tag{A.8}$$

On the other hand, the stiffness matrix of element can be expressed as

$$\mathbf{k}_e = \int_e \mathbf{B}_e^{\mathrm{T}} \mathbf{D} \mathbf{B}_e dv \tag{A.9}$$

where $\mathbf{B}_e$ is 6×48 displacement—strain matrix, in which every element is a quadratic function with respect to *xyz*-monomial or L_{ijmn}-monomial. And $\mathbf{D}$ is 6×6 material constant matrix, reads

$$\mathbf{D} = \begin{bmatrix} d_1 & d_2 & d_2 & 0 & 0 & 0 \\ d_2 & d_1 & d_2 & 0 & 0 & 0 \\ d_2 & d_2 & d_1 & 0 & 0 & 0 \\ 0 & 0 & 0 & d_3 & 0 & 0 \\ 0 & 0 & 0 & 0 & d_3 & 0 \\ 0 & 0 & 0 & 0 & 0 & d_3 \end{bmatrix} \tag{A.10}$$

where $d_1 = E(1-\upsilon)/d$, $d_2 = E\upsilon/d$, $d_3 = E(0.5-\upsilon)/d$, and $d = (1+\upsilon)(1-2\upsilon)$. E and υ are Young's modulus and Poisson's ratio, respectively. For the sake of a simple presentation, $\mathbf{B}_e$ can be written as

$$\mathbf{B}_e = \begin{bmatrix} b_{1,1} & b_{1,2} & \cdots & b_{1,48} \\ b_{2,1} & b_{2,2} & \cdots & b_{2,48} \\ \vdots & \vdots & \ddots & \vdots \\ b_{6,1} & b_{6,2} & \cdots & b_{6,48} \end{bmatrix} \tag{A.11}$$

By combining similar terms of polynomials, in Eq. (A.11) $b_{i,j} (i = 1, 2, \ldots, 6; j = 1, 2, \ldots, 48)$ is a quadratic polynomial, but is not complete. For example, $b_{1,1}$ can be denoted as

$$\begin{aligned} b_{1,1} = {} & B_{1\_1\_2} L_i + B_{1\_1\_6} L_i^2 + B_{1\_1\_7} L_i L_j + B_{1\_1\_9} L_i L_m \\ & + B_{1\_1\_10} L_j L_m + B_{1\_1\_12} L_i L_n + B_{1\_1\_13} L_j L_n + B_{1\_1\_14} L_m L_n \end{aligned} \tag{A.12}$$

where the B-coefficients $B_{1\_1\_2}$, $B_{1\_1\_6}$, …, and $B_{1\_1\_14}$ can be obtained through combining similar terms of polynomials. Moreover, the first and second subscripts represent the row- and column-index of $b_{1,1}$ in $\mathbf{B}_e$, while the third subscript stands for the serial number of the pairing L_{ijmn}-monomial in Eq. (A.3). For $B_{1\_1\_9}$ and $B_{1\_1\_10}$, we give the following illustration:

$$\begin{cases} f_1 = 1 \\ f_2 = L_i \\ \vdots \\ f_9 = L_i L_m \leftrightarrow B_{1\_1\_9} \Rightarrow B_{1\_1\_9} L_i L_m \\ f_{10} = L_j L_m \leftrightarrow B_{1\_1\_10} \Rightarrow B_{1\_1\_10} L_j L_m \\ \vdots \\ f_{210} = L_n^6 \end{cases} \tag{A.13}$$

Therefore, $b_{1,1}$ can be abbreviated to

$$\begin{aligned} b_{1,1} = {} & B_{1\_1\_2} f_2 + B_{1\_1\_6} f_6 + B_{1\_1\_7} f_7 + B_{1\_1\_9} f_9 + B_{1\_1\_10} f_{10} \\ & + B_{1\_1\_12} f_{12} + B_{1\_1\_13} f_{13} + B_{1\_1\_14} f_{14} \end{aligned} \tag{A.14}$$

In like manner, for the integrand of Eq. (A.9), namely,

$$\tilde{\mathbf{k}}_e = \mathbf{B}_e^{\mathrm{T}} \mathbf{D} \mathbf{B}_e \tag{A.15}$$

We can denote $\tilde{\mathbf{k}}_e$ by

$$\tilde{\mathbf{k}}_e = \begin{bmatrix} k_{1,1} & k_{1,2} & \cdots & k_{1,48} \\ k_{2,1} & k_{2,2} & \cdots & k_{2,48} \\ \vdots & \vdots & \ddots & \vdots \\ k_{6,1} & k_{6,2} & \cdots & k_{6,48} \end{bmatrix} \tag{A.16}$$

and $k_{1,1}$ reads

$$\begin{aligned} k_{1,1} = {} & K_{1\_1\_5} f_5 + K_{1\_1\_15} f_{15} + \quad \text{Omit 25 terms} \\ & + K_{1\_1\_63} f_{63} + K_{1\_1\_64} f_{64} + K_{1\_1\_65} f_{65} \end{aligned} \tag{A.17}$$

where the K-coefficients $K_{1\_1\_5}$, $K_{1\_1\_15}, \ldots$, and $K_{1\_1\_65}$ can be obtained via combining similar terms of polynomials.

Up to now, the generation of the element stiffness matrix has been converted into the calculation of the K-coefficients and Eq. (A.8). At the same time, there are several things to note: One, only need to calculate the non-zero elements of $\tilde{\mathbf{k}}_e$; Two, the value of Eq. (A.8) can be repeatedly used for generating the other sub-matrixes involving the integral operation; Three, Eq. (A.8) is applicable to arbitrary shape polyhedron manifold element, while for tetrahedron element one can use the following formula [52]

$$\int_e L_i^a L_j^b L_m^c L_n^d dv = 6V \frac{a!b!c!d!}{(a+b+c+d+3)!} \tag{A.18}$$

to calculation the integration of Lijmn-monomials.

References

[1] Shi GH. Manifold method of material analysis. In: Proceedings of the transactions of the 9th army conference on applied mathematics and computing; 1991. p. 57–76.
[2] Tsay RJ, Chiou YJ, Chuang WL. Crack growth prediction by manifold method. J Eng Mech 1999;125:884–90.
[3] Chiou YJ, Lee YM, Tsay RJ. Mixed mode fracture propagation by manifold method. Int J Fract 2002;114:327–47.
[4] Ma GW, An XM, Zhang HH, Li LX. Modelling complex crack problems using the numerical manifold method. Int J Fract 2009;156:21–35.
[5] Wu ZJ, Wong LNY. Modeling cracking behavior of rock mass containing inclusions using the enriched numerical manifold method. Eng Geol 2013;162:1–13.
[6] Zheng H, Liu F, Li CG. The MLS-based numerical manifold method with applications to crack analysis. Int J Fract 2014;190(1–2):147–66.
[7] Yang SK, Ma GW, Ren XH, Ren F. Cover refinement of numerical manifold method for crack propagation simulation. Eng Anal Bound Elem 2014;43:37–49.
[8] Fan H, Zheng H, Li C, He S. A decomposition technique of generalized degrees of freedom for mixed-mode crack problems. Int J Numer Methods Eng 2017. doi:10.1002/nme.5533.
[9] Zhang ZR, Zhang XW, Yan JH. Manifold method coupled velocity and pressure for Navier–Stokes equations and direct numerical solution of unsteady incompressible viscous flow. Comput Fluids 2010;39(8):1353–65.

[10] Zhang ZR, Zhang XW. Direct simulation of low-Re flow around a square cylinder by numerical manifold method for Navier–Stokes equations. J Appl Math 2012;2012:1–14.
[11] Wang Y, Hu MS, Zhou QL, Rutqvist J. Energy-work-based numerical manifold seepage analysis with an efficient scheme to locate the phreatic surface. Int J Numer Anal Methods Geomech 2014;38:1633–50.
[12] Zheng H, Liu F, Li CG. Primal mixed solution to unconfined seepage flow in porous media with numerical manifold method. Appl Math Model 2015;39(2):794–808.
[13] Zheng H, Liu ZJ, Ge XR. Numerical manifold space of hermitian form and application to kirchhoff's thin plate problems. Int J Numer Methods Eng 2013;95:721–39.
[14] Zhang HH, Ma GW. Fracture modeling of isotropic functionally graded materials by the numerical manifold method. Eng Anal Bound Elem 2014;38:61–71.
[15] Zhang YL, Liu DX, Tan F. Numerical manifold method based on isogeometric analysis. Sci China Technol Sci Ser E 2015;58(9):1520–32.
[16] Babuska I, Melenk JM. The partition of unity method. Int J Numer Methods Eng 1997;40:727–58.
[17] Zhang GX, Yasuhito S, Hiroo H, Wang GL. The second order manifold method with six node triangle mesh. J Struct Mech Earthq Eng 2002;19(1):1–9.
[18] Fan H, He SM, Jiang ZM. A high-order numerical manifold method with nine-node triangular meshes. Eng Anal Bound Elem 2015;61:172–82.
[19] Chen GQ, Ohnishi Y, Ito T. Development of higher-order manifold method. Int J Numer Methods Eng 1998;43:685–712.
[20] An XM, Li LX, Ma GW, Zhang HH. Prediction of rank deficiency in partition of unity-based methods with plane triangular or quadrilateral meshes. Comput Methods Appl Mech Eng 2011;200(5–8):665–74.
[21] An XM, Liu XY, Zhao ZY, He L. Proof of linear independence of flat-top PU-based high-order approximation. Eng Anal Bound Elem 2014;44:104–11.
[22] Cai YC, Zhuang XY, Augarde C. A new partition of unityfinite element free from the linear dependence problem and possessing the delta property. Comput Methods App Mech Eng 2010;199:1036–43.
[23] Zheng H, Xu DD. New strategies for some issues of numerical manifold method in simulation of crack propagation. Int J Numer Methods Eng 2014;97:986–1010.
[24] Fan H, Zheng H, He SM, Jiang ZM. A novel numerical manifold method with derivative degrees of freedom and without linear dependence. Eng Anal Bound Elem 2016;64:19–37.
[25] Qu XL, Fu GY, Ma GW. An explicit time integration scheme of numerical manifold method. Eng Anal Bound Elem 2014;48:53–62.
[26] Chen ZD. On the representation of finite rotation in nonlinear field theory of continuum mechanics. Appl Math Mech 1986;7(11):1017–26.
[27] Li P, Chen ZD. The updated co-moving coordinate formulation of continuum mechanics based on the S–R decomposition theorem. Comput Methods Appl Mech Eng 1994;114:21–34.
[28] Fan H, Zheng H, He SM. S–R decomposition based numerical manifold method. Comput Methods Appl Mech Eng 2016;304:452–78.
[29] Sukumar N, Moës N, Moran B, Belytschko T. Extended finite element method for three-dimensional crack modeling. Int J Numer Methods Eng 2000;48(11):1549–1570.
[30] Duarte CA, Babuka I, Oden JT. Generalized finite element methods for three-dimensional structural mechanics problems. Comput Struct 2000;77(2):215–32.
[31] Rabczuk T, Belytschko T. Adaptivity for structured meshfree particle methods in 2D and 3D. Int J Numer Methods Eng 2005;63(11):1559–82.
[32] Cheng YM, Zhang YH. Formulation of a three-dimensional numerical manifold method with tetrahedron and hexahedron elements. Rock Mech Rock Eng 2008;41(4):601–28.
[33] Jiang QH, Zhou CB, Li DQ. A three-dimensional numerical manifold method based on tetrahedral meshes. Comput Struct 2009;87(13):880–9.
[34] He L, Ma GW. Development of 3D numerical manifold method. Int J Comput Methods 2010;7(01):107–29.
[35] He L, An XM, Ma GW, Zhao ZY. Development of three-dimensional numerical manifold method for jointed rock slope stability analysis. Int J Rock Mech Min Sci 2013;64:22–35.
[36] He L, An XM, Liu XY, Zhao ZY, Yang SQ. Augmented numerical nanifold method with implementation of flat-top partition of unity. Eng Anal Bound Elem 2015;61:153–71.
[37] Wu YQ, Chen GQ, Jiang ZS, Zhang L, Zhang H, Fan FS, et al. Research on fault cutting algorithm of the three-dimensional numerical manifold method. Int J Geomech 2016;17(5) E4016003.
[38] Shi GH. Ph.D. thesis. Berkeley: University of California; 1988.
[39] Fan H, Zheng H, Zhao JD. Discontinuous deformation analysis based on strain-rotation decomposition. Int J Rock Mech Min Sci 2017;92:19–29.
[40] Tian R, Yagawa G. Generalized nodes and high-performance elements. Int J Numer Methods Eng 2005;64:2039–71.
[41] Tian R, Yagawa G, Terasaka H. Linear dependence problems of partition of unity-based generalized FEMs. Comput Methods Appl Mech Eng 2006;195:4768–82.
[42] Ma GW, An XM, He L. The numerical manifold method: a review. Int J Comput Methods 2010;7(1):1–32.
[43] Shi GH. Three dimensional discontinuous deformation analyses. In: Proceedings of the DC Rocks 2001, the 38th US Symposium on Rock Mechanics (USRMS). American Rock Mechanics Association; 2001.
[44] Zienkiewicz OC, Taylor RL, Zhu JZ. The finite element method: Its basis and fundamentals. 7th ed. Butterworth-Heinemann: Elsevier; 2013.
[45] Washizu K. Variational methods in elasticity and plasticity. 3rd ed. New York: Pergamon Press; 1982.
[46] Keast P. Moderate-degree tetrahedral quadrature formulas. Comput Methods Appl Mech Eng 1986;55(3):339–48.
[47] https://people.sc.fsu.edu/~jburkardt/f_src/tetrahedron_keast_rule/tetrahedron_keast_rule.html.
[48] Shi GH. Simplex integration for manifold method, FEM, DDA and analytical analysis. In: Proceedings of the 1st international Forum on Discontinuous Deformation Analysis (DDA) and Simulations of Discontinuous Media. Albuquerque, New Mexico, USA: TSI Press; 1996. p. 205–62.
[49] MacNeal RH, Harder RL. A prop sed standard set of problems to test finite element accuracy. Finite Elem Anal Des 1985;1:3–20.
[50] Cook RD, Malkus DS, Plesha ME. Concepts and applications of finite element analysis. 3rd ed. New York: Wiley; 1989.
[51] Payen DJ, Bathe KJ. Improved stresses for the 4-node tetrahedral element. Comput Struct 2011;89(13):1265–73.
[52] Eisenberg MA, Malvern LE. On finite element integration in natural coordinates. Int J Numer Meth Eng 1973;7:574–5.